https://doi.org/10.5194/egusphere-2026-4866
Preprint. Discussion started: 19 August 2026

Attenuation and Salinity Dominance of Submesoscale Surface Density Gradients in the German Bight

Samuel M Ayim[1] and Oliver Wurl[1]

[1]Center of Marine Sensors (ZfMarS), Institute for Chemistry and Biology of the Marine Environment (ICBM), Carl von Ossietzky University of Oldenburg, 26382 Wilhelmshaven, Germany

Correspondence to: Samuel M. Ayim (samuel.mintah.ayim@uni-oldenburg.de)

Abstract

Submesoscale horizontal density gradients at the ocean surface play a vital role in driving upper-ocean mixing and air-sea exchange. However, horizontal density structures are often assumed to directly reflect the underlying water dynamics. This study presents high-resolution along-track observations collected by the autonomous surface vehicle HALOBATES in the German Bight. The measurements capture co-located horizontal density gradients in both the ocean skin layer, sampled at approximately 80 µm, and the near-surface layer (NSL) at 1 m depth. The results reveal partial decoupling and significant attenuation of horizontal density gradients between the skin and the NSL (slope = 0.41 ± 0.008, R^2 = 0.18), alongside a persistent baseline of skin layer spatial variability that produces a higher front-detection rate than in the NSL (8.3% against 7.2%). Density fronts at the skin are disproportionately salinity-driven rather than temperature-driven (44.1% salinity-only and 33.7% temperature-only), more so than at the NSL (39.9% against 31.8%). Tidal phase significantly modulates gradient intensity at both layers. Random Forest machine learning coupled with SHapley Additive exPlanations identified skin temperature and salinity as the dominant predictors of gradient intensity, while atmospheric pressure, wind speed, and air-sea temperature difference contributed substantially. Nevertheless, predictive skill across the full range of gradient intensities remained limited (test R^2 = 0.19). These findings demonstrate that submesoscale density gradients at the skin layer can decouple substantially from underlying upper-ocean structures. This vertical disconnect highlights potential biases in satellite validation and proxy-based approaches that rely on sea-surface skin measurements to infer submesoscale dynamics in complex coastal waters.

https://doi.org/10.5194/egusphere-2026-4866
Preprint. Discussion started: 19 August 2026

1. Introduction

The oceanic skin layer, or sea surface microlayer, forms the dynamic boundary interface between the ocean and atmosphere (Ribas-Ribas et al., 2017; Wurl et al., 2024). It directly modulates air–sea exchanges of heat and gases, surfactant accumulation, and micro-scale wave dissipation. Despite its pivotal role in global biogeochemical cycles and upper-ocean thermodynamics, observational oceanography has historically relied on bulk or near-surface layer (NSL, 1 m depth) measurements collected at depths of 1 to 10 m via moorings, research vessels, or FerryBox automated monitoring networks (Grayek et al., 2011). While satellite remote sensing provides broad spatial coverage, it lacks the temporal continuity, cloud-free reliability, and vertical resolving power needed to continuously sample fine-scale gradients between the skin and underlying water column (Minnett et al., 2019).

Submesoscale processes operating on horizontal scales of 100 m to 50 km are characterized by intense spatial gradients, buoyant plume dynamics, lateral straining, and strong localized vertical motion (Capet et al., 2008; D'Asaro et al., 2011; McWilliams, 2016; Su et al., 2018). In shallow, tidally energetic coastal environments like the German Bight in the southeastern North Sea (Hagen et al., 2022), submesoscale variability is further modulated by complex interactions between tidal straining, seasonal thermal stratification, and major estuarine freshwater discharge from the Elbe, Weser, and Ems rivers (Simpson and Hunter, 1974). Existing submesoscale frameworks are typically defined under the implicit assumption that horizontal gradients observed within the NSL pass unimpeded to the absolute surface skin layer. This assumption is rarely tested directly because of the lack of instrumentation required to do so and having co-located, high-frequency skin and NSL sensors sampled along a moving platform that deliberately re-crosses the same feature. Satellite climatologies have been used to detect submesoscale fronts (Belkin et al., 2009; Belkin and O'Reilly, 2009), but they inherently treat the retrieved skin temperature as a proxy for the underlying frontal structure. This assumption is convenient for basin-scale mapping but has seldom been validated at the along-track, sub-kilometre resolution where submesoscale processes generate fronts. Ground-truthing this assumption requires a platform that can both sample the skin layer directly, at the few-hundreds of micrometres scale the skin layer occupies. The platform must also repeatedly transect an observed front rather than sampling it once in passing, a capability that most moored, drifting, or single-pass shipboard sensors cannot provide.

However, the air–sea interface is continuously subjected to latent evaporation, solar radiation heating, wind-driven shear stress, and organic surfactant activity (Donlon et al., 2002; Fairall et al., 1996; Wurl et al., 2011). These boundary-layer mechanisms establish a distinct thermal

https://doi.org/10.5194/egusphere-2026-4866
Preprint. Discussion started: 19 August 2026

and haline skin effect. Whether submesoscale horizontal density fronts in the NSL undergo attenuation, structural deformation, or enhancement at the surface skin layer remains a fundamental open question in physical oceanography. Furthermore, assessing whether these shallow coastal density fronts are primarily governed by thermal or haline drivers, and identifying the meteorological thresholds that control front formation is vital for refining submesoscale ocean models and improving satellite calibration algorithms. A front that is haline-driven carries no direct thermal signature and is therefore invisible to infrared satellite retrieval regardless of how well that retrieval is calibrated against skin temperature. A front that is thermally driven but strongly attenuated between the NSL and the skin will be under-represented in satellite imagery relative to its true sub-surface intensity. Both possibilities have direct consequences for how confidently a satellite-derived frontal product can be used to infer sub-surface density structure, biological aggregation, or air–sea flux anomalies in a shallow shelf sea. Similarly, if front formation and persistence are gated by identifiable, non-linear thresholds in wind speed, tidal phase, or air–sea temperature difference, those thresholds become directly actionable. They specify the meteorological conditions under which a satellite-based or model-based frontal product should be trusted, and the conditions under which it should not.

Our study utilizes high-resolution along-track data collected by the Autonomous Surface Vehicle (ASV) HALOBATES (Wurl et al., 2024) across five research cruises over 54 cruise-days in the German Bight to understand the density gradients of the sea surface, its dynamics and to identify forcing factors. By analysing co-located skin and NSL measurements at 1-minute temporal intervals and approximately 150 m along-track distance, we address three primary research questions. First, how do horizontal gradients of density at the skin layer scale with and diverge from co-located gradients within the NSL? Additionally, what are the dominant thermohaline drivers governing horizontal density, salinity and temperature gradients in the German Bight, and how are these regimes modulated across distinct tidal phases? Finally, which meteorological and hydrographic variables exert the strongest predictive control on skin layer density gradient, and what non-linear environmental thresholds govern front persistence and dissipation?

https://doi.org/10.5194/egusphere-2026-4866
Preprint. Discussion started: 19 August 2026

2. Methods

2.1 Study Area

Data were collected over 54 cruise-days during five research cruises in the German Bight (Figure 1b), south-eastern North Sea (Figure 1a). The study area is a shallow, tidally energetic shelf sea with an established history of tidal-front and FerryBox-based surface monitoring (Grayek et al., 2011). The expeditions were conducted on the research vessel (RV) Heincke with data from the cruises HE598 in May 2022 (Gassen et al., 2024a), HE609 in October 2022 (Gassen et al., 2025), HE614 in March 2023 (Gassen et al., 2024b), HE626 in July/August 2023 (Ayim et al., 2025a), HE644 in July 2024 (Ayim et al., 2026b). All data are available on the PANGAEA data repository with the references above for the individual cruises.

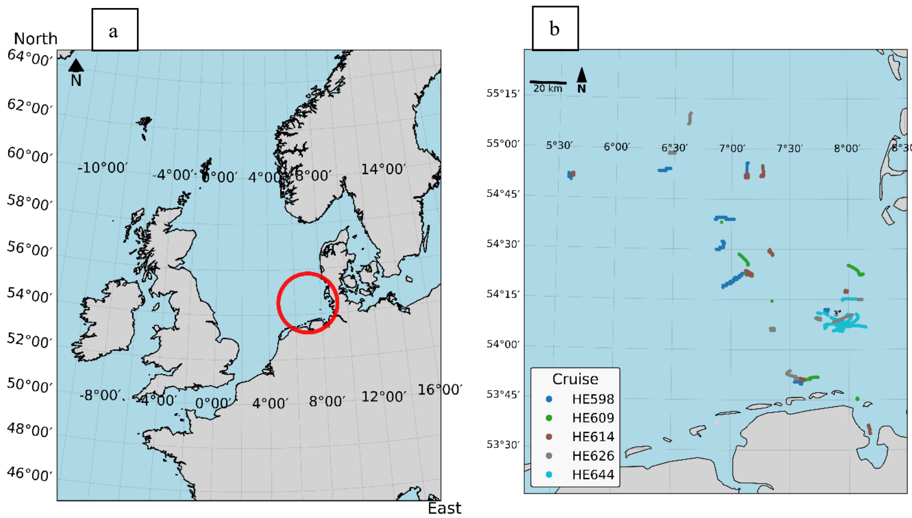

Figure 1: Study Area with stations across the 5 cruises in the German Bight. (a) is the map of the North Sea with the red circle highlighting the study area. (b) is the zoomed in study area showing the locations of the five research cruises.

2.2 Device and Data

HALOBATES is equipped with a rotating glass disc assembly that allows the sampling of the skin layer (78 ± 8.8 µm) of the sea surface due to surface tension and adhesion (Ribas-Ribas et al., 2017; Shinki et al., 2012; Wurl et al., 2024). The glass disc assembly is covered with a tinted acryl glass hood to avoid evaporative cooling at stronger winds as some biases without hood were observed during validation with an infrared radiometer (see figure 2 in (Wurl et al., 2019)). HALOBATES has a ladder at the bow with temperature and pressure sensors and sampling tubes for the flow-through conductivity-temperature-depth (CTD) sensors mounted on the

https://doi.org/10.5194/egusphere-2026-4866
Preprint. Discussion started: 19 August 2026

ASV. The maximum depth sampled was 1 meter. The meteorological sensors are mounted on the bridge of the ASV at a height of 2 m measuring wind speed and direction, atmospheric pressure, relative humidity and air temperature. Other meteorological sensors were mounted on the ship which was averagely at a 500 m distance from the ASV, this includes net shortwave and longwave radiation, precipitation intensity and amount.

The longitude, latitude and time were logged continuously. The raw dataset comprised 101,645 timestamped data points at 10 second resolution. Data spans various events such as front, rain, slicks and days without any apparent surface phenomena. The CTDs (OS310, Idrounat, Italy) had temperature and conductivity accuracy of ± 0.0015 °C and ± 0.003 mS/cm, respectively. A detailed description of the design and capabilities of HALOBATES are reported in the technical paper of the ASV (Wurl et al., 2024). On a typical front day, we observed the phenomenon by going back and forth across the ocean feature (Figure 2). The TPXO-OSU model (Egbert et al., 1994; Egbert and Erofeeva, 2002) was then used to obtain tidal record based on the date, time and geolocation details of HALOBATES.

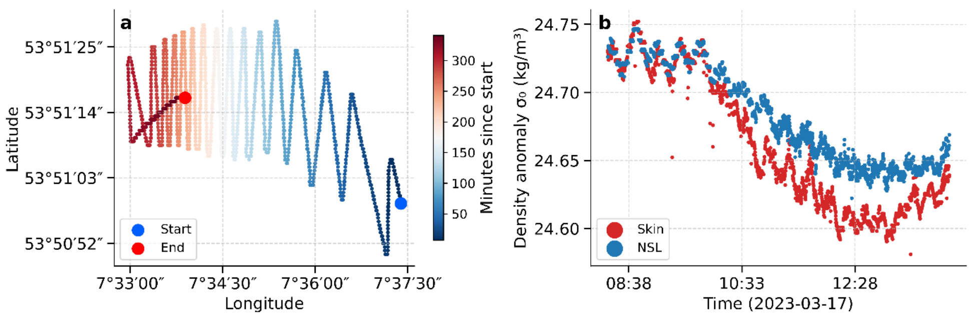

Figure 2: A typical track (a) and Density anomaly (b) as we moved back and forth across an observed front.

2.3 Data Quality

Raw samples were passed through a quality control (QC) scheme, with valid data row counts logged at every stage. First, we took out October 12, 2022 as the skin layer salinity had long periods of outliers and a few of the other sensors having no data. We also removed all rows and time points where any of the four-core variables (skin and NSL temperature and salinity) had a missing value. Due to the knowledge of the region's oceanography, a salinity minimum of 28 g kg^{-1} was set to exclude false data by bubbles in the conductivity cell. Due to the focus on gradients, we filtered out sensor spikes between consecutive measurements. To do so, we have used a threshold of 0.03 °C and 0.03 g/kg for the temperature and salinity respectively. That is,

https://doi.org/10.5194/egusphere-2026-4866
Preprint. Discussion started: 19 August 2026

we have excluded values that exceed the previous value by this threshold within the 10 second data interval. This threshold was chosen after testing different thresholds and evaluating the effect on the whole dataset. Data were then resampled to a strict 1-minute grid, computed independently within each day. The resampling used a first principle by taking the first value of the minute and not the mean which will average the gradient intensities. Along-track distance was computed via the haversine formula between consecutive 1-minute positions; a data row was retained for gradient analysis if the time gap was $<=$ 70 s and the along-track distance fell between 0 and 360 m. The distance limits used is based on the maximum distance we expect the ASV to cover in one minute.

After QC and resampling, 73,617 data points remained, and 14,446 one-minute data points were produced, of which 13,029 (90.2%) were valid because the time and distance difference fulfilled the criteria. Based on examination of the raw data and the pre-processed data, a targeted salinity-spike guard was applied after gradient-intensity computation. Raw salinity gradient intensities exceeding 0.2 g/kg, that is approximately 7 times the salinity front-detection threshold, were considered implausible as a true salinity gradient between consecutive 1-minute measurements. In addition, in cases where the skin and NSL salinity gradient intensity disagreed by more than 0.11 g/kg were treated as sensor artefacts. This threshold was chosen through visual inspection of the time-series. Such events occurred in isolation without a smooth transition of the gradients during such time periods and thus where treated as outliers. The salinity-spike guard and the threshold for the difference between skin and NSL salinity flagged 101 data points (0.70%).

2.4 Density and Front Computations

Density was computed from temperature and conductivity via the TEOS-10 gsw toolbox (McDougall and Barker, 2011; UNESCO/IOC et al., 2010). Gradient intensity was defined as the absolute difference between consecutive 1-minute measurements. We intentionally retained this raw temporal difference rather than calculating a distance-normalized gradient, as linear extrapolation across a full kilometre is physically invalid for fine submesoscale features (McWilliams, 2016). Each step in our data corresponds to 1 minute and approximately 150 m. We compute the density ratio Rp (Eq. 1) to assess the thermal and haline contribution of the observed density gradients. The density ratio is based on the thermal expansion α and the β saline contraction coefficients (Schmitt, 1981). To distinguish strong dominance from near-compensated conditions, stratification was operationally categorized into haline-dominated ($R\rho < 0.67$), thermally-dominated ($R\rho > 1.5$), and mixed ($0.67 \leq R\rho \leq 1.5$) regimes. These represents

https://doi.org/10.5194/egusphere-2026-4866
Preprint. Discussion started: 19 August 2026

a minimum 1.5-fold (or 60%) relative contribution of one variable over the other (Ruddick, 1983; Rudnick and Martin, 2002).

$$\boldsymbol{R\rho} = \frac{\boldsymbol{\alpha}|\Delta \boldsymbol{T}|}{\boldsymbol{\beta}|\Delta \boldsymbol{S}|} \tag{1}$$

In this study, a front is defined by the density gradient-intensity threshold (>= 0.02 kg m^{-3}) as a fixed, reproducible cut-off. This threshold was based on a number of factors. First, we primarily looked at the literature and found density gradient of 0.2 – 2.0 kg m^{-3} per km in San Diego (Wu et al., 2021). When this is scaled down to a 100 m distance, this gives density gradients of 0.02 – 0.2 kg m^{-3} per 100 m. We then visually inspected the days where we could clearly see a front and found this threshold to be true for our dataset. Also, when we computed the percentiles, this value sits around the 90th percentile. Density is the dynamically relevant quantity as it drives the convergence or divergence associated with a front (Capet et al., 2008; McWilliams, 2016). This makes it the appropriate primary detector, particularly given the well-documented tendency of temperature and salinity gradients to compensate one another's effect on density rather than simply add (Rudnick and Ferrari, 1999). Given a detected density front, temperature (>= 0.03 ° C) and salinity (>= 0.02 g kg^{-1}) gradient conditions are then checked for co-occurrence and classified as T and S (both conditions independently met), T only, S only, or neither fulfilled the criteria. This detection approach is conceptually distinct from the widely used gradient and histogram-based algorithms developed for satellite SST/chlorophyll imagery (Belkin et al., 2009; Belkin and O'Reilly, 2009), but adapted here to a 1-D along-track shipboard record rather than a 2-D image. Tidal phase was classified from the sign of the within-day first difference of tidal height: positive indicates the rising tide, negative indicates falling tide, and a small-magnitude of the tidal height difference $\Delta h < 1e^{-4}$ m indicates a tidal slack. The rising and falling tide are thus referred to as Flood and Ebb tide respectively.

2.5 Machine Learning and SHapley Additive exPlanations attribution

To explore meteorological and hydrographic predictor variables as best predictors for gradient intensity, a random-forest regressor (Breiman, 2001) was trained to predict continuous skin density gradient intensity. Two sets of variables were compared: the first set includes tidal height, wind speed and direction, air-sea temperature difference, relative humidity, net shortwave and longwave radiation, atmospheric pressure, skin temperature, skin salinity, and a

https://doi.org/10.5194/egusphere-2026-4866
Preprint. Discussion started: 19 August 2026

cyclic time-of-day encoding. The second set excludes shortwave and longwave radiation. Radiation fields carry substantially more missing values than the other variables, and an initial full-feature run found radiation had the lowest SHAP importance of any variable, so the second set is treated as the primary model, trading a small amount of potential signal for a much larger usable sample. Models were evaluated with a 75/25 train-test split, with performance assessed directly on the holdout test set using the coefficient of determination (R^2), root-mean-square error (RMSE) bias. SHAP (SHapley Additive exPlanations; (Lundberg and Lee, 2017)) values from a tree explainer were used to rank feature importance and to visualise partial dependence for the top predictors. We tested group differences across tidal phase with the Kruskal-Wallis test. The paired skin against NSL comparison were tested with the Wilcoxon signed-rank since skin and NSL gradient intensity are measured on the same along-track step and are therefore not independent data.

3. Results

For context, density gradient intensity is strongly heavy-tailed as shown in Figure 3. The median is 0.004 kg m^{-3}, but the 95th, 99th, and 99.9th percentiles are 0.028, 0.057, and 0.106 kg m^{-3}, respectively. The most intense data points (0.1% of all datapoints) are roughly 25 times the median. Most of the along-track record are below the fixed front-detection threshold of 0.02 kg m^{-3} (dashed line in Figure 3) highlighting that crossing into a true front is the exception rather than the rule, consistent with submesoscale straining events that are localised in space and time.

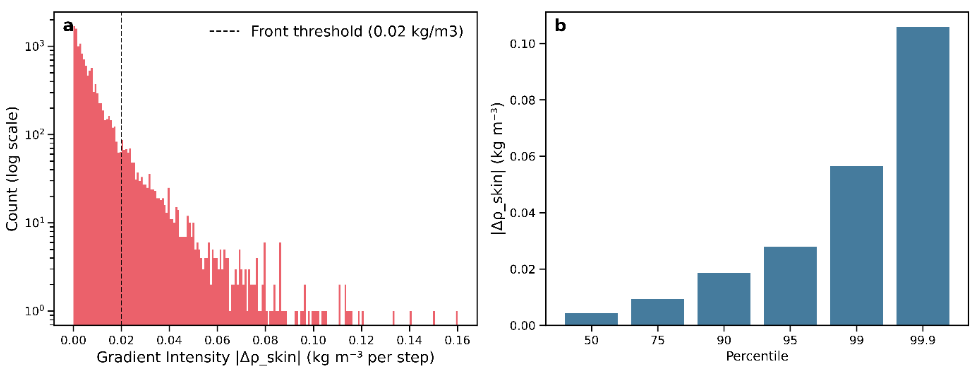

Figure 3:(a) Distribution of skin density gradient intensity (log-scale count), with the fixed front-detection threshold marked. (b) Percentiles of the same distribution, illustrating the heavy tail.

https://doi.org/10.5194/egusphere-2026-4866
Preprint. Discussion started: 19 August 2026

3.1 Difference between gradients at the skin and NSL

Using density as the primary front-detection variable, we identified 1192 skin fronts (8.3% of valid steps) and 1035 NSL fronts (7.2%), distributed across all five campaigns. To evaluate how the density gradients, differ from each other, we evaluated matched step-by-step observations by comparing the skin and NSL layers (Figure 4). We treat NSL gradient intensity as the independent (predictor) variable and skin gradient intensity as the dependent (response) variable, consistent with our physical framing of the skin layer as an attenuated surface expression of the underlying bulk signal, and quantify this relationship using Ordinary Least Squares (OLS) linear regression (Figure 4a). The regression slope ($m = 0.409 \pm 0.008$) falls well below the 1:1 line of equal intensity ($m = 1.0$), demonstrating substantial attenuation of the skin front compared to the sub-surface fronts at 1 meter depth. On average, a 1.00 kg m^{-3} increase in gradient intensity at the NSL corresponds to an increase of approximately 0.41 kg m^{-3} at the skin layer. The regression's positive intercept ($c = 0.005$ kg m^{-3}) highlights a persistent background baseline level of spatial variability maintained at the skin layer even when NSL waters are completely homogeneous, while its low coefficient of determination ($R^2 = 0.179$) indicates that NSL dynamics explain less than 18% of the variance in skin gradient intensity. The Bland-Altman analysis reveals that this vertical coupling is regime dependent (Figure 4b). During times of low mean gradient < 0.02 kg m $^{-3}$, paired differences are close to zero, indicating that skin and NSL layers track each other closely in weak gradient conditions. During a strong frontal regime (mean gradient > 0.04 kg m^{-3}), the two layers diverge sharply with differences between layers ranging from -0.14 kg m^{-3} to 0.11 kg m^{-3}.

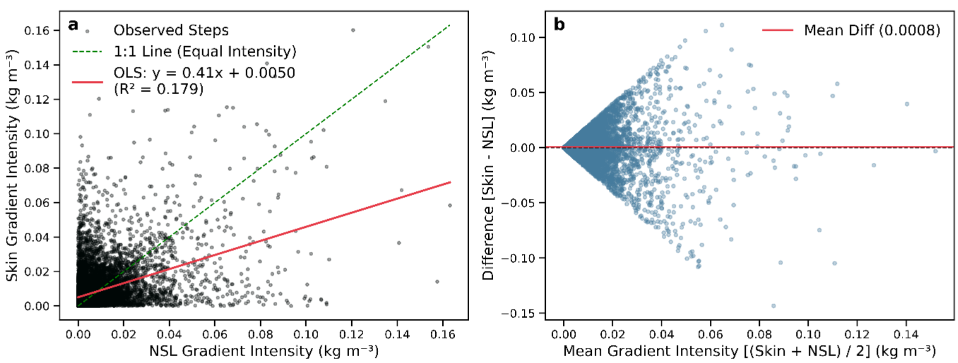

Figure 4: Scaling and alignment between ocean skin and NSL density gradient intensities. (a) Scatter plot and Ordinary Least Squares (OLS) linear regression. The solid red line demonstrates gradient attenuation relative to the 1:1 reference line (black dashed). (b) Bland-Altman plot of paired differences versus mean gradient intensity. Mean paired difference is shown by the red horizontal line.

https://doi.org/10.5194/egusphere-2026-4866
Preprint. Discussion started: 19 August 2026

3.2 Tidal Phase influence on gradients

Gradient intensities were compared across flood (n = 6,836), ebb (n = 6,186), and phases of slack water (n = 183), representing 13,205 one-minute observations (Table 1). Kruskal–Wallis tests revealed significant tidal effects on all skin layer gradients: temperature ($H(2) = 24.13$), salinity ($H(2) = 52.49$), and density ($H(2) = 27.25$) with all p-values $\ll 0.001$. Salinity exhibited the strongest tidal dependence, indicating that tidal modulation primarily influenced horizontal salinity structure (Figure 5). Flood tide produced the largest mean skin gradients for temperature (0.020 ± 0.032 °C), salinity (0.008 ± 0.012 g kg^{-1}), and density (0.008 ± 0.012 kg m^{-3}). Skin density gradients were approximately 22% larger than those at NSL (0.007 kg m^{-3}) during flood tide. Skin and NSL density gradients were identical with a value of 0.007 kg m^{-3} during ebb tide. Density fronts ($|\Delta\rho| \geq 0.02$ kg m^{-3}) occurred most frequently during flood tide (10.4%), compared with ebb (7.6%) and phases of slack water (6.6%). The vertical temperature difference (ΔT = skin – NSL) remained positive throughout all tidal phases, with the strongest warming during flood tide (0.079 ± 0.273 °C). Dunn's post-hoc test showed that flood tide differed significantly from both ebb tide ($p < 0.001$) and phases of slack water ($p = 0.028$), but ebb and slack water were not significantly different ($p = 0.395$). It indicates that the principal tidal contrast was associated with enhanced density gradients during flood tides.

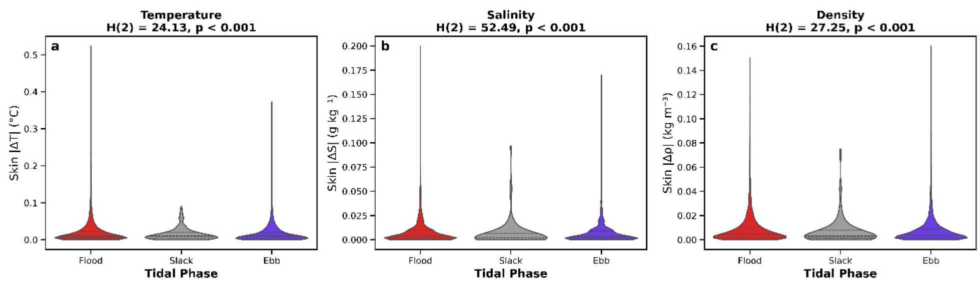

Figure 5: Violin plots of gradients in absolute values of skin (a) temperature, (b) salinity, and (c) density during flood, slack water, and ebb tidal phases (N = 13,205). Dashed and dotted lines denote the median and interquartile range. Kruskal–Wallis statistics demonstrate significant tidal dependence for all variables, with salinity exhibiting the strongest response. Summary statistics are provided in Table 1.

https://doi.org/10.5194/egusphere-2026-4866
Preprint. Discussion started: 19 August 2026

Table 1: Skin and NSL gradient properties across tidal phases. Values are reported as mean ± standard deviation.

Tidal phase	Skin $|\Delta T|$ (°C)	Skin $|\Delta S|$ (g kg^{-1})	Skin $|\Delta\rho|$ (kg m^{-3})	NSL $|\Delta\rho|$ (kg m^{-3})	Front rate (Skin, %)	Front rate (NSL, %)	n
Flood	0.020 ± 0.032	0.008 ± 0.012	0.009 ± 0.012	0.007 ± 0.011	10.4	7.7	6,836
Slack	0.015 ± 0.017	0.006 ± 0.013	0.007 ± 0.010	0.005 ± 0.009	6.6	3.8	183
Ebb	0.016 ± 0.022	0.007 ± 0.012	0.007 ± 0.011	0.007 ± 0.010	7.6	8.1	6,186

3.3 Gradients and Environmental Factors

We assessed the thermal and haline contributions to the observed density gradients. We determine the percentage of density fronts occurring at the same time as salinity front, temperature front or neither, that is, cases where the density front was driven by sub-threshold contributions from both variables jointly. Detection thresholds for the co-occurrence of temperature and salinity fronts (Figure 6) reveals a clear asymmetry: at the skin layer, 44.1% of density fronts are salinity-driven, 33.7% are temperature-driven, 21.1% show both, and only 1.0% show neither individually crossing its threshold. At the NSL, the separation is closer: 39.9% salinity-only, 31.8% temperature-only, 27.8% both. Salinity gradients are therefore the dominant contributor to density fronts at the skin compared to the NSL in the North Sea.

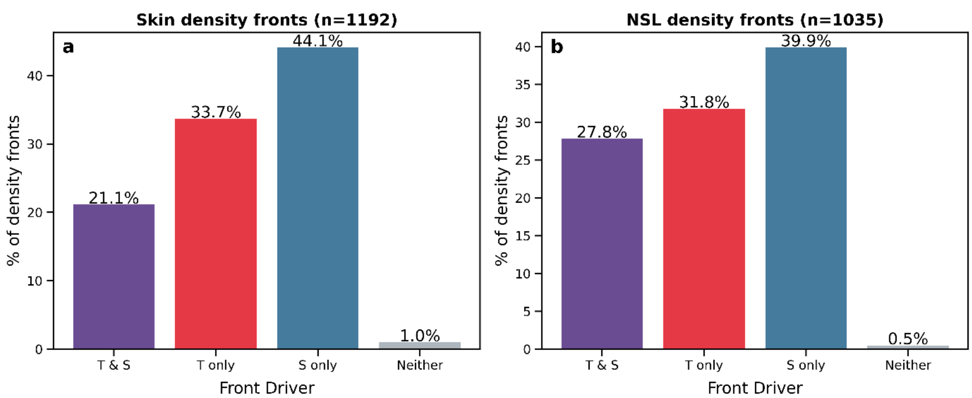

Figure 6: Temperature/salinity co-occurrence at detected density fronts, skin (a) vs. NSL (b).

This is corroborated by a continuous thermal/haline dominance-ratio classification using the same gradient-intensity terms (Figure 7a). Haline dominance represents the largest proportion of observations (approximately 55–60%) across flood and ebb tides and slack waters, followed

https://doi.org/10.5194/egusphere-2026-4866
Preprint. Discussion started: 19 August 2026

by thermal (20–25%) and mixed (15–20%) regimes. The distribution shows minor changes with tidal phases, indicating that the relative influence of temperature and salinity gradients is largely independent of tidal state. Thermally dominated fronts occur mainly when winds are < 8 m s^{-1}, where the density ratio exhibits a broad range of values (Figure 7b). As wind speed increases, observations shift toward haline dominance, consistent with stronger turbulent mixing reducing horizontal thermal gradients while salinity gradients remain comparatively persistent. Most observations under a cooler atmosphere, that is air temperature is below sea surface temperature, fall within the haline and mixed regimes (Figure 7c). Thermal dominance occurs primarily when the atmosphere is slightly warmer than the sea surface (by approximately 0 – 2.5 °C), consistent with conditions favouring stable oceanic near-surface thermal stratification. Overall, salinity is the dominant control on density gradients (Figure 7a), whereas thermal dominance occurs primarily at wind speed < 8 m s^{-1} (Figure 7b) and positive air–sea temperature differences (Figure 7c).

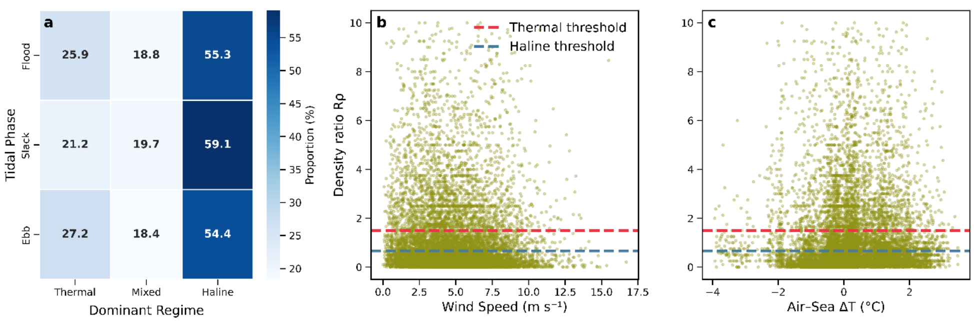

Figure 7: Thermal vs. haline dominance regime: (a) proportion by tidal phase, (b) regime vs. wind speed, (c) regime vs. air-sea temperature difference, coloured by tidal height

We binned wind speed into four ranges: <2 m s^{-1} (calm, slick-favourable), 2–6 m s^{-1} (transitional), 6–8 m s^{-1} (approaching the wave-breaking threshold), and >8 m s^{-1} (mixing-dominated). This partitioning combines field observations showing substantially reduced surface roughness in surfactant-rich coastal waters relative to the open ocean at wind speeds below 4 m s^{-1} (Laxague et al., 2024), consistent with visual observations during our own cruises of the sea surface losing its characteristic smoothness once wind speeds exceed ~2 m s^{-1}, with threshold behaviour reported in laboratory wind-wave tank experiments (Engel et al., 2026), and with established thresholds for surfactant slick persistence (Romano, 1996; Wurl et al., 2011). The lowest wind speed bin (<2 m s^{-1}) shows a higher mean skin |Δρ| of 0.013 kg m^{-3} (Figure 8c), more variability and a front-detection rate of 19.4% which is roughly 2.3–3.4 times

https://doi.org/10.5194/egusphere-2026-4866
Preprint. Discussion started: 19 August 2026

higher than the 2–6 m s^{-1} (8.5%), 6–8 m s^{-1} (5.7%), and >8 m s^{-1} (7.6%) bins. Rainfall was flagged in 7.7% of valid one-minute steps (993 of 12,928). Skin density gradient intensity was significantly lower during rain than during dry conditions (Mann-Whitney U = 4,886,105, $p < 0.001$). The median skin $|\Delta\rho|$ fell from 0.005 kg m^{-3} (no rain) to 0.003 kg m^{-3} (rain) (Figure 8b), and the skin front-detection rate fell from 9.65% (no rain) to 4.03% (rain). This pattern held within every tidal phase examined, with rain-conditional medians lower than dry-conditional medians.

We also investigated whether the gradient intensities varied across the seasons, that is the cruises (Figure 8a). Skin density gradient intensity differs sharply and significantly across cruises (Kruskal–Wallis H = 969.4, $p << 0.001$). A Dunn's post-hoc test showed that four of the five cruises are statistically distinguishable from nearly every other cruise with all pairwise $p < 0.005$ except between HE598 (May 2022) and HE614 (Octobe$^{r\,2}$022) with p = 0.13. The two summer cruises, HE626 (July/August 2023) and HE644 (July 2024) showed the highest median and mean skin gradient intensity (0.007 and 0.006 kg m^{-3} median, respectively) and the highest front-detection rates (14.7% and 11.9%), while the autumn cruise HE609 (October 2022) shows the lowest of both (0.002 kg m^{-3} median, 4.4% front-detection rate).

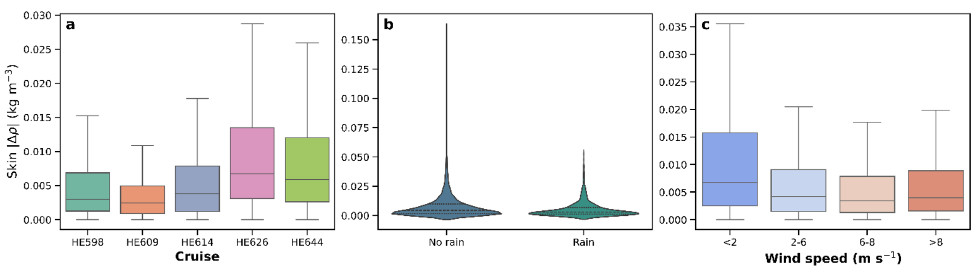

Figure 8: Distribution of density gradients across the skin layer. (a) Boxplot of Skin $|\Delta\rho|$ across five research cruises (HE598 [May], HE609 [October], HE614 [March], and HE626, HE644 [July/August]). (b)Violin plot showing the probability density distribution of Skin $|\Delta\rho|$ during dry (No rain) versus precipitating (Rain) conditions. (c) Boxplot of Skin $|\Delta\rho|$ grouped by wind speed regimes. For the boxplots, horizontal lines denote the median, boxes span the interquartile range (IQR), and whiskers represent the data spread. In the violin plots, dotted lines inside the distributions indicate the median and quartiles.

The influence of radiation variables on gradient intensity prediction was initially evaluated to capture potential diurnal warming effects. However, by including radiation parameters the data set is substantially reduced from 12,367 to 4,003 observations due to incomplete data. Radiation inclusion did not improve model performance. The full model achieved a low test $R^2 = 0.082$ compared with the model excluding radiation of $R^2 = 0.188$. Therefore, the no-radiation model

https://doi.org/10.5194/egusphere-2026-4866
Preprint. Discussion started: 19 August 2026

was selected as the primary model due to the larger number of observations (N = 12,367) and improved predictive performance.

The model performance showed a low overall bias (+0.0001 kg m^{-3}) and an RMSE of 0.0097 kg m^{-3}. Interpretation of these metrics must consider the strongly right-skewed distribution of observed skin layer density gradients (Figure 3a), which exhibited a median of 0.0040 kg m^{-3} and a mean of 0.0080 kg m^{-3}. The difference between mean and median reflects the influence of relatively rare, high-intensity gradient events on the overall distribution. The model's mean absolute error (MAE = 0.0058 kg m^{-3}) remained below the observed mean gradient intensity, indicating that typical prediction errors were comparable to the background variability of the dataset. However, the RMSE exceeded both the observed mean (121%) and median (241%) since squared-error metrics give disproportionate weight to large residuals associated with extreme gradient events. Observed versus predicted comparisons (Figure 9) showed good agreement along the 1:1 relationship under low-to-moderate gradient conditions ($\Delta\rho < 0.02$ kg m^{-3}), though scatter around the 1:1 line indicates that individual predictions in this regime can deviate substantially even where aggregate error metrics are low, reflecting irreducible case-by-case variability rather than systematic bias. However, the model systematically underestimated the largest observed gradients exceeding 0.04 kg m^{-3} by more than 50%. This limitation reflects the difficulty of predicting transient, localized but extreme skin layer density gradient using atmospheric and hydrographic predictors.

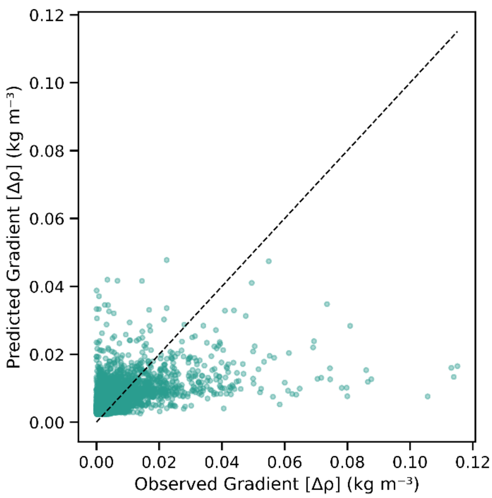

Figure 9: Predicted vs. observed skin gradient intensity for the regressor model (N = 3,092 test samples). The black dashed line represents the 1:1 line of perfect agreement.

https://doi.org/10.5194/egusphere-2026-4866
Preprint. Discussion started: 19 August 2026

SHAP analysis identified surface hydrographic variables as the dominant control of density gradient intensity (Figure 10). Skin temperature was the most influential predictor (mean |SHAP| ≈ 0.0023 kg m⁻³), followed by skin salinity (≈0.0018 kg m⁻³). Atmospheric pressure and wind speed were the most important atmospheric predictors. The analysis revealed that high skin temperatures generally increased predicted gradient intensity, while low salinity values produced strong positive SHAP contributions, indicating enhanced gradients under fresher conditions (Figure 10). In contrast, increasing wind speed generally reduced predicted gradient intensity, consistent with increased mixing and reduced persistence of sharp surface gradients. Partial dependence analysis (Figure 11) revealed distinct non-linear relationships between predictors and predicted gradient intensity. Skin temperature showed relatively weak effects between 5 and 17 °C, followed by a rapid increase in predicted gradient intensity above 17 °C and exceeding 0.022 kg m⁻³ at 22 °C. Skin salinity showed the strongest response under low-salinity conditions between 29 and 30 g kg^{-1} in which predicted gradients levelled up to approximately 0.033 kg m⁻³. Density gradients declined toward a baseline of ~0.010 kg m⁻³ at higher salinities (>33 g kg^{-1}). For atmospheric drivers, wind speed showed the clearest threshold behaviour. Gradient intensity was highest under near-zero winds (>0.016 kg m⁻³) and rapidly decreased between 2 and 4 m s⁻¹, reaching a stable minimum (~0.008 kg m⁻³) above 5 m s⁻¹. Atmospheric pressure exhibited a weaker response, with elevated gradients under low-pressure conditions (<1005 hPa) and minimum values between approximately 1012 and 1018 hPa.

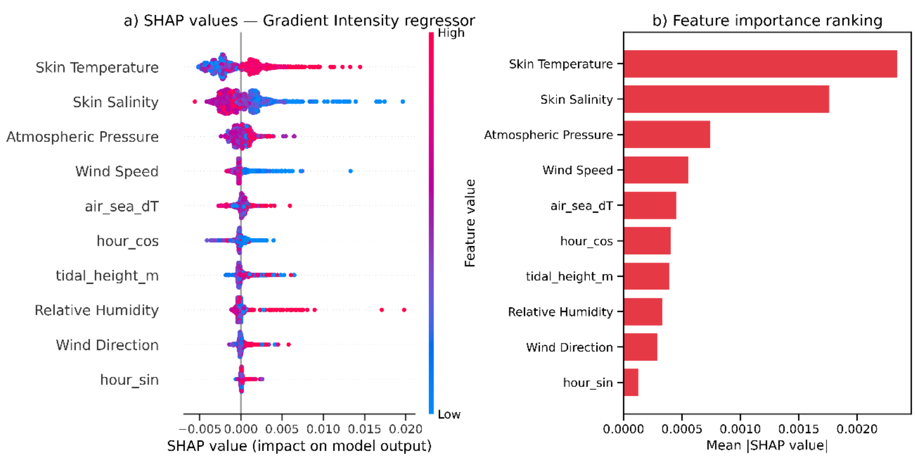

Figure 10: Feature importance and directional attribution of environmental predictors governing density gradient intensity using SHAP (SHapley Additive exPlanations) values. (a) SHAP summary plot showing feature value impact on model predictions. Points are coloured by feature magnitude (red = high, blue = low). (b) Global feature importance ranking sorted by mean absolute SHAP value.

https://doi.org/10.5194/egusphere-2026-4866
Preprint. Discussion started: 19 August 2026

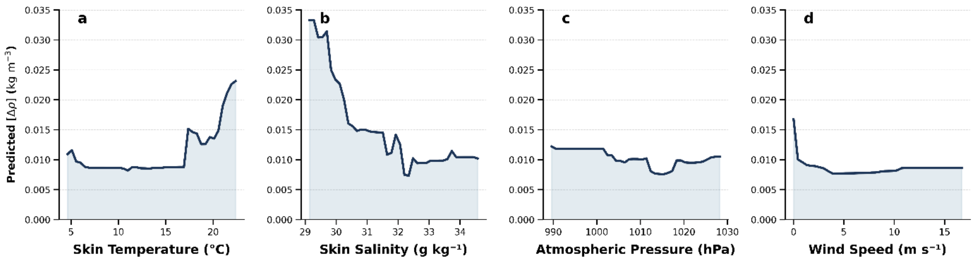

Figure 11: Partial dependence plots displaying the marginal, non-linear effects of the top four environmental drivers on predicted density gradient intensity: Skin Temperature, Skin Salinity, Atmospheric Pressure, and Wind Speed.

4. Discussion

4.1 Vertical Decoupling and Gradient Attenuation

Our empirical findings of attenuated and weakly-coupled surface gradients that diverge under strong frontal forcing demonstrate a partial decoupling and significant attenuation of horizontal oceanographic gradients across the upper metre of the ocean column. Our analysis on paired linear regression between skin and NSL density gradient intensities (Figure 4a) indicates that, on average, a sub-surface horizontal density gradient is attenuated by roughly 60% at the sea surface skin layer. Furthermore, sub-surface gradient dynamics account for less than 18% of the total variance observed in surface skin gradients, indicating that the ocean skin layer operates as a dynamic, and only partially decoupled physical regime rather than a passive and separated top boundary. The Bland–Altman analysis confirms that this vertical alignment is strongly regime-dependent. In conditions of small horizontal gradients ($|\Delta\rho| < 0.02$ kg m^{-3}), skin and NSL gradient intensities maintain tight equilibrium, tracking each other with near-zero mean bias. However, at stronger frontal regime ($|\Delta\rho| > 0.04$ kg m^{-3} per step), the two layers diverge sharply, with inter-layer differences spreading widely. This divergence during intense frontogenesis is explained by upper-ocean fluid dynamics and thermodynamic boundary processes (McWilliams, 2016; Thomas et al., 2008). For example, submesoscale fronts are characterized by convergent surface velocity fields that force opposing water masses together, driving downward subduction and sharp lateral shear in the bulk upper mixed layer (Capet et al., 2008; D'Asaro et al., 2011). At the skin layer, however, this lateral convergence competes directly with vertical air–sea heat fluxes, evaporation, and surfactant-induced Marangoni surface tension gradients (Donlon et al., 2002; Ribas-Ribas et al., 2017). These micro-surface processes damp localized density contrasts, resulting in a smoothed spatial profile relative to the underlying flow.

The positive regression intercept (c = 0.005 kg m⁻³, Figure 4a) underscores another key physical behaviour. When bulk waters at 1 m depth are spatially homogeneous (Δρ NSL = 0), a baseline level of horizontal spatial variability is maintained across the skin layer. This micro-spatial baseline might be sustained by localized, patchy atmospheric exchanges, micro-scale wind stress variations, and organic surfactant slicks that alter local evaporation rates independently of sub-surface hydrodynamics (Ribas-Ribas et al., 2017). The attenuation is related to the higher absolute front-detection rate at the skin (8.3%) than at the NSL (7.2%). The regression and attenuation describe different aspects of the same regime-dependent coupling. The OLS slope characterises the typical relationship between the layers, which is dominated by the very large number of weak, near-zero steps where skin and NSL track closely as seen in Figure 4a. The front-detection rate, by contrast, is a threshold-crossing statistic driven by the tail of the distribution, where the positive intercept's baseline skin variability is large enough on its own to push a skin gradient over the fixed 0.02 kg m⁻³ threshold even when the co-located NSL gradient does not. That is, even though the skin layer understates the intensity of most gradients, its constant micro-fluctuations under low sea states force it over low fixed thresholds more frequently overall.

4.2 Tidal Hydrodynamics and Thermohaline Dominance Regimes

Tidal forcing acts as a key hydrodynamic control on horizontal oceanographic structure across the German Bight (Otto et al., 1990; Schrum, 1997). Non-parametric Kruskal–Wallis tests confirmed significant variations across tidal phases for skin temperature, salinity, and density. Salinity exhibited the strongest tidal sensitivity, underscoring that tidal modulation in this shallow shelf sea primarily reorganizes freshwater boundaries rather than thermal fields. Flood tides yielded the sharpest horizontal gradients and the highest density front-detection frequency. During flood tide, denser offshore North Sea water flows landward, pushing directly against buoyant estuarine plumes originating from the Elbe, Weser, and Ems rivers (Grayek et al., 2011; Hagen et al., 2022). This opposing flow sharpens horizontal density boundaries via tidal straining and advective frontogenesis. Conversely, during ebb tides, buoyant estuarine freshwater flows offshore over denser open-sea water as an unconstrained surface plume, leading to broader, more diffuse horizontal transitions and lower front detection rates (Horner-Devine et al., 2015).

Evaluating thermohaline driver co-occurrence at detected density fronts revealed a strong asymmetry (Figure 6). At the skin interface, majority of the density fronts were driven by

https://doi.org/10.5194/egusphere-2026-4866
Preprint. Discussion started: 19 August 2026

salinity only, followed by temperature and the combined thermohaline gradients. Haline dominance consistently accounted for 55–60% of all valid observations across all tidal states, whereas thermal dominance comprised 20–25% and mixed regimes 15–20%. These empirical observations align with mixed-layer thermohaline compensation principles (Ferrari and Rudnick, 2000; Rudnick and Ferrari, 1999). In shallow shelf seas, horizontal temperature gradients are continually damped by air–sea heat exchange through latent, sensible, and radiative heat fluxes (Donlon et al., 2002), whereas horizontal salinity gradients lack a rapid restoring atmospheric flux (Ferrari and Rudnick, 2000), allowing fresh estuarine runoff to maintain persistent spatial density contrasts.

4.3 Environmental Thresholds and Predictive Machine Learning

Skin density gradient intensity is governed by a set of identifiable, non-linear environmental thresholds spanning wind speed, season, and rainfall, which together set the physical background for the predictive machine-learning. Wind speed exerts the clearest threshold behaviour. Binning wind speed showed that skin density gradient intensity and front-detection rate are both far higher under calm conditions (< 2 m s^{-1}) and decay rapidly as wind forcing increases. This is consistent with field observations showing that surface roughness is substantially suppressed in surfactant-rich waters below 4 m s^{-1} (Laxague et al., 2024), allowing persistent, sharp-edged surfactant patches and their associated density signatures to survive rather than being dispersed by wind-driven turbulence. The partitioning of the wind speeds corresponds to independently documented physical thresholds for surfactant behaviour at the sea surface. Field observations demonstrate that distinct bacterioneuston communities and organic surfactant enrichments in the SML collapses above a sharp threshold of 5.6 m s^{-1} (Rahlff et al., 2017). This agrees with wind-wave tank experiments showing a breakdown of biopolymer SML enrichment at wind speeds above 6 m s^{-1} (Engel et al., 2026), corresponding precisely to the 6–8 m s^{-1} wind bin in our dataset where gradient intensity and front detection rates reached their lowest levels.

Below 5 m s^{-1}, natural surfactant films are known to damp capillary and short gravity waves substantially, visually appearing as slicks (Romano, 1996; Wurl et al., 2011). A patch of surfactant-damped surface water bounded by a sharp edge represent small-scale, non-advective feature. This can inflate both the mean gradient intensity and the front-detection rate specifically under low wind conditions, independent of the tidal and thermohaline forcing discussed above. The regime classification supports this finding as the proportion of thermally-dominated observations is highest under calm winds (33.2%) and declines under stronger winds. This is

https://doi.org/10.5194/egusphere-2026-4866
Preprint. Discussion started: 19 August 2026

consistent with thin, thermally stratified, surfactant-stabilised surface patches that persist only under low to no turbulent conditions. We note that this dataset carries no independent optical or visual slick flag, so the wind-bin evidence here is physically-motivated and consistent with, rather than a direct confirmation of, slick presence.

The two summer deployments (HE626, July/August 2023; HE644, July 2024) showed the highest median gradient intensity and front rates, and the autumn cruise (HE609, October 2022) the lowest. This is consistent with the seasonality of stratification in the German Bight Region of Freshwater Influence (ROFI) (Chegini et al., 2020). Strong stratification occurs in spring and early summer, driven by peak Elbe and Weser discharge from snowmelt and seasonal rainfall interacting with the spring–neap tidal cycle (Chegini et al., 2020). During these times, the along-track horizontal density gradient across the Elbe–Weser plume boundary can locally reach magnitudes of up to 1 kg m^{-3} over a few hundred metres under strong plume conditions (Kopte et al., 2022). Conversely, the skin density gradient intensity was significantly lower during rainfall than under dry conditions.

These mechanistic interpretations are corroborated by our Random Forest regression and SHAP attribution analysis (Breiman, 2001; Lundberg and Lee, 2017). Wind speed and atmospheric pressure emerged as the two primary meteorological predictors of gradient intensity. Partial dependence analysis predicted gradient intensity peaks under near-zero wind speed (> 0.016 kg m^{-3}), declines rapidly between 2 and 4 m s^{-1}, and stabilises at a low baseline above 5 m s^{-1}. This 5 m s^{-1} inflection matches the established threshold for rain-driven skin stratification disruption (Gassen et al., 2024c) and the destabilization of the SML (Rahlff et al., 2017). Atmospheric pressure showed a comparatively muted but non-monotonic relationship in the partial dependence analysis, with predicted gradient intensity highest at lower pressures. In terms of hydrographic predictors, skin temperature showed a steep non-linear increase in predicted gradient intensity above 17 °C, peaking near 22 °C, consistent with the summer-cruise seasonal signal identified above. Because surface tension decreases monotonically with temperature (Nayar et al., 2014) localized solar warming in summer skin layers can generate thermal Marangoni stresses (Soloviev and Lukas, 2014). Under low wind conditions, these surface-tension gradients damp micro-turbulent dispersion and maintain sharp horizontal thermal gradients across the skin interface, consistent with the observed increase in predicted gradient intensity at higher skin temperatures. Skin salinity exerted its strongest effect in the least saline water masses (29–30 g kg^{-1}), consistent with proximity to the Elbe–Weser plume boundary (Kopte et al., 2022). The complexity collaborated the convergence of the SHAP ranking, the

https://doi.org/10.5194/egusphere-2026-4866
Preprint. Discussion started: 19 August 2026

partial-dependence thresholds, and the independently-established physical thresholds for surfactant collapse, rain-driven stratification, and plume-driven seasonality. Our findings provide predictive results as a mechanistic foundation as it would not have as a standalone statistical fit.

4.4 Broader Scientific Implications for Remote Sensing and Air–Sea Fluxes

These empirical findings have direct implications for satellite oceanography and climate modelling. Infrared satellite sensors sample thermal radiation from the ocean skin layer, at a depth of 10 – 20 µm, whereas microwave sensors integrate radiation over a much greater depth of ~1 cm known as the subskin layer with signal decaying exponentially with depth (Donlon et al., 2002). Front-detection algorithms applied to satellite imagery (Belkin and O'Reilly, 2009) assume that detected surface gradients accurately reflect underlying water structures (Ayim et al., 2025b, 2026a; Vazquez-Cuervo et al., 2019). Our results show that sub-surface fronts are attenuated by roughly 60% at the skin interface and diverge significantly during strong frontal processes. Consequently, satellite-derived gradient intensities likely underestimate the true magnitude of underlying submesoscale fronts in shallow shelf seas. Furthermore, global climate models parameterize air–sea heat and momentum exchange using bulk sea surface measurements taken at 1 to 5 m depth (Fairall et al., 1996). The vertical partial decoupling observed in our study confirms that the skin layer maintains its unique spatial variability. Neglecting this micro-surface variability may introduce biases into calculated air–sea flux budgets, particularly during low-wind regimes (< 5 m s^{-1}) where skin gradients are most pronounced.

The wind-speed threshold identifies the specific meteorological regime (calm, <2 m s^{-1}) in which skin layer gradient structure is least representative of, and widely decoupled from, the sub-surface field. Studies on satellite validations would typically use sub-surface characteristics as ground truth due to the lack of "true" surface data. We have discussed the need of ocean skin data for satellite validation in previous studies (Ayim et al., 2025b, 2026a). Validation campaigns timed to calm, clear-sky conditions may therefore be systematically sampling the regime of largest skin/NSL disagreement, and not the smallest. That is true in frontal zones as shown in this study. The inter-cruise analysis shows that a single research cruise, even so using state-of-the-art instrumentations, may not capture a representative tidal-phase relationship. This is highlighted by the reversal observed during HE614 and the well-documented seasonal modulation of German Bight ROFI stratification (Chegini et al., 2020; Kopte et al., 2022).

https://doi.org/10.5194/egusphere-2026-4866
Preprint. Discussion started: 19 August 2026

Multi-season validation campaigns, or explicit seasonal stratification of validation statistics, are needed before generalising a tidal correction factor derived from any single deployment.

5. Conclusion

This study demonstrates that submesoscale horizontal density gradients undergo partial vertical decoupling and attenuation between the ocean skin and the NSL. High-resolution along-track measurements from the autonomous surface vehicle HALOBATES in the tidally energetic German Bight reveal that surface skin gradients do not consistently mirror underlying water dynamics, and that this decoupling is disproportionately carried by salinity rather than temperature. Tidal phase is a significant modulator of gradient intensity, and machine learning analysis via Random Forest models and SHAP attribution identified atmospheric pressure, wind speed, and air-sea temperature difference as predictors of gradient intensity parallel to the expected dominant hydrographic predictor of temperature and salinity.

Despite these key findings, several limitations should be considered. The observational dataset is geographically restricted to the shallow, tidally energetic waters of the German Bight, meaning the observed environmental thresholds may differ in open-ocean regimes or other coastal environments. Sampling was limited to five specific deployment windows across two years; the March 2023 cruise, notably, reversed the pooled tidal-phase pattern seen in the other four cruises. This underscores that the tidal mechanism proposed here is likely conditional on seasonal estuarine stratification state rather than universal and may not be fully captured by our seasonal sampling design. The Random Forest model's low explanatory power ($R^2 = 0.19$) and its systematic under-prediction of the largest observed gradients indicate that the SHAP-ranked drivers should be considered as relative importance among measured variables rather than a complete explanation of gradient intensity. Addressing these limitations through expanded multi-platform campaigns, continuous vertical profiling, and multi-season deployment will be essential for refining remote sensing validation strategies and improving submesoscale frontogenesis models.

Data availability

All data are freely available at the data repository PANGAEA as follows. Digital object identifiers are available for processed data from the HALOBATES.

HE598; https://doi.org/10.1594/PANGAEA.968799.

HE609; https://doi.org/10.1594/PANGAEA.968800.

HE614; https://doi.org/10.1594/PANGAEA.969378.

HE626; https://doi.org/10.1594/PANGAEA.972989.

HE644; https://doi.org/10.1594/PANGAEA.989737.

Author contributions

OW and SMA conceptualized the ideas. SMA curated the data, conducted formal analysis and investigation, developed the methodology and the prepared the original draft and visualisation. OW acquired the funding, managed the project, provided the resources, supervised and reviewed and edited the manuscript.

Competing interests

The authors declare that they have no conflict of interest.

Acknowledgements

We thank the Lower Saxony Ministry of Science and Culture (MWK) for funding this project. We also thank the German Research foundation (DFG) for funding the SCANS and BASS cruises on the RV Heincke. We thank the crew and ship coordination of the RV Heincke for helping with the operations of HALOBATES during the missions, including deployment and recovery. We thank colleagues in our workshop for the maintenance of the mechanical structures of HALOBATES. We are also grateful to the science team on the RV Heincke for their support in the deployment and recovery of HALOBATES.

Financial support

https://doi.org/10.5194/egusphere-2026-4866
Preprint. Discussion started: 19 August 2026

This research ("The North Sea from Space: Using Explainable Artificial Intelligence to Improve Satellite Observations of Climate Change (NorthSat-X)") was funded by the Lower Saxony Ministry of Science and Culture, grant number VWZN3680.

References

Ayim, S. M., Bibi, R., Cortés, E., Gassen, L., Jaeger, L., Lehners, C., Ribas-Ribas, M., and Wurl, O.: High-resolution measurements of essential climate variables in the North Sea from the autonomous surface vehicle HALOBATES during RV Heincke cruise HE626 [dataset]. PANGAEA, https://doi.org/10.1594/PANGAEA.972989, 2025a.

Ayim, S. M., Gassen, L., Ribas-Ribas, M., and Wurl, O.: Skin Temperature of the North Sea from an Autonomous Surface Vehicle Compared to Remote Sensing Observation, Remote Sensing, 17, 4056, https://doi.org/10.3390/rs17244056, 2025b.

Ayim, S. M., Jaeger, L., Gassen, L., and Wurl, O.: Evaluating Satellite and Model Sea Surface Salinity With in Situ Observation from an Autonomous Surface Vehicle, IEEE J. Sel. Top. Appl. Earth Observations Remote Sensing, 19, 20531–20544, https://doi.org/10.1109/JSTARS.2026.3702896, 2026a.

Ayim, S. M., Cortés-Espinoza, E. F., Gassen, L., Jaeger, L., Lehners, C., Rauch, C., and Wurl, O.: High-resolution measurements of essential climate variables in the North Sea from the autonomous surface vehicle HALOBATES during RV Heincke cruise HE644, https://doi.org/10.1594/PANGAEA.989737, 2026b.

Belkin, I. M. and O'Reilly, J. E.: An algorithm for oceanic front detection in chlorophyll and SST satellite imagery, Journal of Marine Systems, 78, 319–326, https://doi.org/10.1016/j.jmarsys.2008.11.018, 2009.

Belkin, I. M., Cornillon, P. C., and Sherman, K.: Fronts in Large Marine Ecosystems, Progress in Oceanography, 81, 223–236, https://doi.org/10.1016/j.pocean.2009.04.015, 2009.

Breiman, L.: Random Forests, Machine Learning, 45, 5–32, https://doi.org/10.1023/A:1010933404324, 2001.

Capet, X., McWilliams, J. C., Molemaker, M. J., and Shchepetkin, A. F.: Mesoscale to Submesoscale Transition in the California Current System. Part III: Energy Balance and Flux, Journal of Physical Oceanography, 38, 2256–2269, https://doi.org/10.1175/2008JPO3810.1, 2008.

Chegini, F., Holtermann, P., Kerimoglu, O., Becker, M., Kreus, M., Klingbeil, K., Gräwe, U., Winter, C., and Burchard, H.: Processes of Stratification and Destratification During An Extreme River Discharge Event in the German Bight ROFI, JGR Oceans, 125, e2019JC015987, https://doi.org/10.1029/2019JC015987, 2020.

D'Asaro, E., Lee, C., Rainville, L., Harcourt, R., and Thomas, L.: Enhanced Turbulence and Energy Dissipation at Ocean Fronts, Science, 332, 318–322, https://doi.org/10.1126/science.1201515, 2011.

Donlon, C. J., Minnett, P. J., Gentemann, C., Nightingale, T. J., Barton, I. J., Ward, B., and Murray, M. J.: Toward Improved Validation of Satellite Sea Surface Skin Temperature Measurements for Climate Research, J. Climate, 15, 353–369, https://doi.org/10.1175/1520-0442(2002)015%3C0353:TIVOSS%3E2.0.CO;2, 2002.

Egbert, G. D. and Erofeeva, S. Y.: Efficient Inverse Modeling of Barotropic Ocean Tides, J. Atmos. Oceanic Technol., 19, 183–204, https://doi.org/10.1175/1520-0426(2002)019%3C0183:EIMOBO%3E2.0.CO;2, 2002.

Egbert, G. D., Bennett, A. F., and Foreman, M. G. G.: TOPEX/POSEIDON tides estimated using a global inverse model, J. Geophys. Res., 99, 24821–24852, https://doi.org/10.1029/94JC01894, 1994.

Engel, A., Friedrichs, G., Krall, K. E., and Jähne, B.: Wind-induced collapse of the biopolymeric surface microlayer induces sudden changes in sea surface roughness, Biogeosciences, 23, 2101–2117, https://doi.org/10.5194/bg-23-2101-2026, 2026.

Fairall, C. W., Bradley, E. F., Godfrey, J. S., Wick, G. A., Edson, J. B., and Young, G. S.: Cool-skin and warm-layer effects on sea surface temperature, J. Geophys. Res., 101, 1295–1308, https://doi.org/10.1029/95JC03190, 1996.

Ferrari, R. and Rudnick, D. L.: Thermohaline variability in the upper ocean, J. Geophys. Res., 105, 16857–16883, https://doi.org/10.1029/2000JC900057, 2000.

https://doi.org/10.5194/egusphere-2026-4866
Preprint. Discussion started: 19 August 2026

Gassen, L., Ayim, S. M., Emig, S., Goßmann, I., Holthusen, L. A., Jaeger, L., Lagemann, M., Lehners, C., Ribas-Ribas, M., and Wurl, O.: High-resolution measurements of essential climate variables in the North Sea from the autonomous surface vehicle HALOBATES during RV Heincke cruise HE598, https://doi.org/10.1594/PANGAEA.968799, 2024a.

Gassen, L., Ayim, S. M., Bibi, R., Cortés, E., Holthusen, L. A., Jaeger, L., Lagemann, M., Lehners, C., Ribas-Ribas, M., and Wurl, O.: High-resolution measurements of essential climate variables in the North Sea from the autonomous surface vehicle HALOBATES during RV Heincke cruise HE614, https://doi.org/10.1594/PANGAEA.969378, 2024b.

Gassen, L., Ayim, S. M., Badewien, T. H., Ribas-Ribas, M., and Wurl, O.: Wind speed effects on rainfall-induced salinity and temperature anomalies at the sea surface microlayer at mid-latitudes, Elem Sci Anth, 12, 00004, https://doi.org/10.1525/elementa.2024.00004, 2024c.

Gassen, L., Ayim, S. M., Emig, S., Holthusen, L. A., Jaeger, L., Lagemann, M., Lehners, C., Ribas-Ribas, M., and Wurl, O.: High-resolution measurements of essential climate variables in the North Sea from the autonomous surface vehicle HALOBATES during RV Heincke cruise HE609, https://doi.org/10.1594/PANGAEA.968800, 2025.

Grayek, S., Staneva, J., Schulz-Stellenfleth, J., Petersen, W., and Stanev, E. V.: Use of FerryBox surface temperature and salinity measurements to improve model based state estimates for the German Bight, Journal of Marine Systems, 88, 45–59, https://doi.org/10.1016/j.jmarsys.2011.02.020, 2011.

Hagen, R., Winter, C., and Kösters, F.: Changes in tidal asymmetry in the German Wadden Sea, Ocean Dynamics, 72, 325–340, https://doi.org/10.1007/s10236-022-01509-9, 2022.

Horner-Devine, A. R., Hetland, R. D., and MacDonald, D. G.: Mixing and Transport in Coastal River Plumes, Annu. Rev. Fluid Mech., 47, 569–594, https://doi.org/10.1146/annurev-fluid-010313-141408, 2015.

Kopte, R., Becker, M., Holtermann, P., and Winter, C.: Tides, Stratification, and Counter Rotation: The German Bight ROFI in Comparison to Other Regions of Freshwater Influence, JGR Oceans, 127, e2021JC018236, https://doi.org/10.1029/2021JC018236, 2022.

Laxague, N. J. M., Zappa, C. J., Soumya, S., and Wurl, O.: The suppression of ocean waves by biogenic slicks, J. R. Soc. Interface., 21, 20240385, https://doi.org/10.1098/rsif.2024.0385, 2024.

Lundberg, S. and Lee, S.-I.: A Unified Approach to Interpreting Model Predictions, https://doi.org/10.48550/ARXIV.1705.07874, 2017.

McDougall, T. J. and Barker, P. M.: Getting Started with TEOS-10 and the Gibbs Seawater (GSW) Oceanographic Toolbox, SCOR/IAPSO Working Group 127, 2011.

McWilliams, J. C.: Submesoscale currents in the ocean, Proc. R. Soc. A., 472, 20160117, https://doi.org/10.1098/rspa.2016.0117, 2016.

Minnett, P. J., Alvera-Azcárate, A., Chin, T. M., Corlett, G. K., Gentemann, C. L., Karagali, I., Li, X., Marsouin, A., Marullo, S., Maturi, E., Santoleri, R., Saux Picart, S., Steele, M., and Vazquez-Cuervo, J.: Half a century of satellite remote sensing of sea-surface temperature, Remote Sensing of Environment, 233, 111366, https://doi.org/10.1016/j.rse.2019.111366, 2019.

Nayar, K. G., Panchanathan, D., McKinley, G. H., and Lienhard, J. H.: Surface Tension of Seawater, Journal of Physical and Chemical Reference Data, 43, 043103, https://doi.org/10.1063/1.4899037, 2014.

Otto, L., Zimmerman, J. T. F., Furnes, G. K., Mork, M., Saetre, R., and Becker, G.: Review of the physical oceanography of the North Sea, Netherlands Journal of Sea Research, 26, 161–238, https://doi.org/10.1016/0077-7579(90)90091-T, 1990.

Rahlff, J., Stolle, C., Giebel, H.-A., Brinkhoff, T., Ribas-Ribas, M., Hodapp, D., and Wurl, O.: High wind speeds prevent formation of a distinct bacterioneuston community in the sea-surface microlayer, FEMS Microbiology Ecology, 93, https://doi.org/10.1093/femsec/fix041, 2017.

Ribas-Ribas, M., Hamizah Mustaffa, N. I., Rahlff, J., Stolle, C., and Wurl, O.: Sea Surface Scanner (S3): A Catamaran for High-Resolution Measurements of Biogeochemical Properties of the Sea Surface Microlayer, Journal of Atmospheric and Oceanic Technology, 34, 1433–1448, https://doi.org/10.1175/JTECH-D-17-0017.1, 2017.

https://doi.org/10.5194/egusphere-2026-4866
Preprint. Discussion started: 19 August 2026

Romano, J.-C.: Sea-surface slick occurrence in the open sea (Mediterranean, Red Sea, Indian Ocean) in relation to wind speed, Deep Sea Research Part I: Oceanographic Research Papers, 43, 411–423, https://doi.org/10.1016/0967-0637(96)00024-6, 1996.

Ruddick, B.: A practical indicator of the stability of the water column to double-diffusive activity, Deep Sea Research Part A. Oceanographic Research Papers, 30, 1105–1107, https://doi.org/10.1016/0198-0149(83)90063-8, 1983.

Rudnick, D. L. and Ferrari, R.: Compensation of Horizontal Temperature and Salinity Gradients in the Ocean Mixed Layer, Science, 283, 526–529, https://doi.org/10.1126/science.283.5401.526, 1999.

Rudnick, D. L. and Martin, J. P.: On the horizontal density ratio in the upper ocean, Dynamics of Atmospheres and Oceans, 36, 3–21, https://doi.org/10.1016/S0377-0265(02)00022-2, 2002.

Schmitt, R. W.: Form of the Temperature-Salinity Relationship in the Central Water: Evidence for Double-Diffusive Mixing, J. Phys. Oceanogr., 11, 1015–1026, https://doi.org/10.1175/1520-0485(1981)011%3C1015:FOTTSR%3E2.0.CO;2, 1981.

Schrum, C.: Thermohaline stratification and instabilities at tidal mixing fronts: results of an eddy resolving model for the German Bight, Continental Shelf Research, 17, 689–716, https://doi.org/10.1016/S0278-4343(96)00051-9, 1997.

Shinki, M., Wendeberg, M., Vagle, S., Cullen, J. T., and Hore, D. K.: Characterization of adsorbed microlayer thickness on an oceanic glass plate sampler, Limnology & Ocean Methods, 10, 728–735, https://doi.org/10.4319/lom.2012.10.728, 2012.

Simpson, J. H. and Hunter, J. R.: Fronts in the Irish Sea, Nature, 250, 404–406, https://doi.org/10.1038/250404a0, 1974.

Soloviev, A. and Lukas, R.: The Near-Surface Layer of the Ocean: Structure, Dynamics and Applications, Springer Netherlands, Dordrecht, https://doi.org/10.1007/978-94-007-7621-0, 2014.

Su, Z., Wang, J., Klein, P., Thompson, A. F., and Menemenlis, D.: Ocean submesoscales as a key component of the global heat budget, Nat Commun, 9, 775, https://doi.org/10.1038/s41467-018-02983-w, 2018.

Thomas, L. N., Tandon, A., and Mahadevan, A.: Submesoscale processes and dynamics, in: Geophysical Monograph Series, vol. 177, edited by: Hecht, M. W. and Hasumi, H., American Geophysical Union, Washington, D. C., 17–38, https://doi.org/10.1029/177GM04, 2008.

UNESCO/IOC, SCOR, and IAPSO: The International Thermodynamic Equation of Seawater – 2010: Calculation and Use of Thermodynamic Properties, UNESCO, 2010.

Vazquez-Cuervo, J., Gomez-Valdes, J., Bouali, M., Miranda, L., Van Der Stocken, T., Tang, W., and Gentemann, C.: Using Saildrones to Validate Satellite-Derived Sea Surface Salinity and Sea Surface Temperature along the California/Baja Coast, Remote Sensing, 11, 1964, https://doi.org/10.3390/rs11171964, 2019.

Wu, X., Feddersen, F., and Giddings, S. N.: Characteristics and Dynamics of Density Fronts over the Inner to Midshelf under Weak Wind Conditions, Journal of Physical Oceanography, 51, 789–808, https://doi.org/10.1175/JPO-D-20-0162.1, 2021.

Wurl, O., Wurl, E., Miller, L., Johnson, K., and Vagle, S.: Formation and global distribution of sea-surface microlayers, Biogeosciences, 8, 121–135, https://doi.org/10.5194/bg-8-121-2011, 2011.

Wurl, O., Landing, W. M., Mustaffa, N. I. H., Ribas-Ribas, M., Witte, C. R., and Zappa, C. J.: The Ocean's Skin Layer in the Tropics, JGR Oceans, 124, 59–74, https://doi.org/10.1029/2018JC014021, 2019.

Wurl, O., Gassen, L., Badewien, T. H., Braun, A., Emig, S., Holthusen, L. A., Lehners, C., Meyerjürgens, J., and Ribas, M. R.: HALOBATES: An autonomous surface vehicle for high-resolution mapping of the sea-surface microlayer and near-surface layer on essential climate variables, Journal of Atmospheric and Oceanic Technology, https://doi.org/10.1175/JTECH-D-24-0021.1, 2024.